

Implantable Beta Radiation Detecting Active Pixel Sensor Design For Prostate Cancer Surveillance

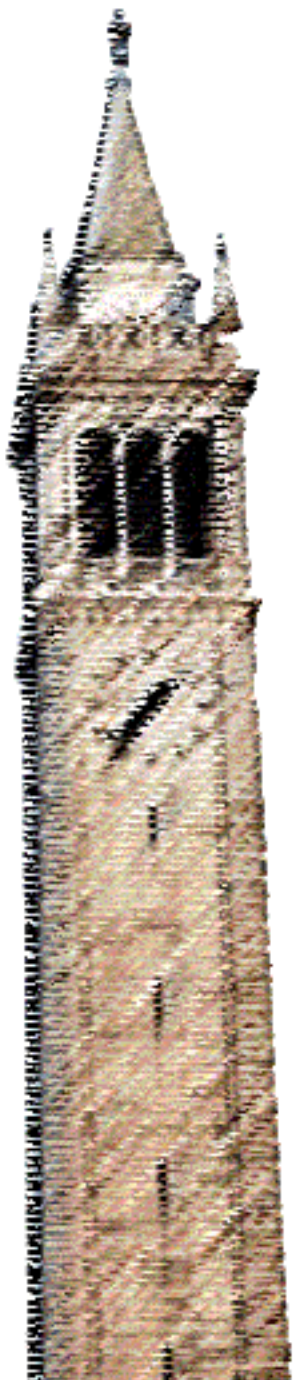
*Leticia Ibarra
Michel Maharbiz
Kristofer Pister*

Electrical Engineering and Computer Sciences
University of California at Berkeley

Technical Report No. UCB/EECS-2017-177

<http://www2.eecs.berkeley.edu/Pubs/TechRpts/2017/EECS-2017-177.html>

December 1, 2017



Copyright © 2017, by the author(s).
All rights reserved.

Permission to make digital or hard copies of all or part of this work for personal or classroom use is granted without fee provided that copies are not made or distributed for profit or commercial advantage and that copies bear this notice and the full citation on the first page. To copy otherwise, to republish, to post on servers or to redistribute to lists, requires prior specific permission.

Acknowledgement

This work was made possible through the research collaborations with UCSF Associate Professor Mekhail Anwar, UCSF Radiation and Oncology Research group, and the Washington State Department of Radiology and Biomedical imaging. This research effort would not be possible without the wise guidance and support from my research advisor, Kristofer S.J. Pister, who is credited with developing the stacked Active Pixel Sensor design idea. I would also like to thank my co-advisor Michel M. Maharbiz, who has been an active supporter of the project design, and Stefanie Garcia, my research partner and supporter. Special thanks for anyone taking interest in this project report.

Implantable Beta Radiation Detecting Active Pixel Sensor Design
for Prostate Cancer Surveillance

By

Leticia Ibarra

A project report submitted in partial satisfaction of the requirements for the degree of Master of
Science, Plan II, in Electrical Engineering in the Graduate Division of the University of
California, Berkeley, Fall 2015

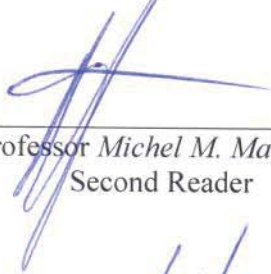
Committee:



Professor *Kristofer S.J. Pister*
Research Advisor

12/18/15

Date



Professor *Michel M. Maharbiz*
Second Reader

12/18/2015

Date

Acknowledgements

This work was made possible through the research collaborations with UCSF Associate Professor *Mekhail Anwar*, UCSF Radiation and Oncology Research group, and the Washington State Department of Radiology and Biomedical imaging. This research effort would not be possible without the wise guidance and support from my research advisor, *Kristofer S.J. Pister*, who is credited with developing the stacked Active Pixel Sensor design idea. I would also like to thank my co-advisor *Michel M. Maharbiz*, who has been an active supporter of the project design, and *Stefanie Garcia*, my research partner and supporter. Special thanks for anyone taking interest in this project report.

Abstract

Monitoring for cancer recurrence after initial therapy is challenging. Current imaging technology limits the size at which cancer may be detected; currently, the smallest clinically detectable tumor is 1-2 mm in diameter [1,20]. A locally recurrent tumor of this size has a high chance for metastatic dissemination, which could render the patient incurable [2]. In collaboration with oncologist researchers from Washington State University and UC-San Francisco, we propose a modern cancer surveillance technique that utilizes a radiation-detecting micro-sensor employed with radiolabeled inhibitor-based anti-body drug conjugates (ADC's) for the localization of prostate cancer. To achieve molecular identification and localization, a network of CMOS image sensors will be used to localize tumor growth at early stages. As preliminary design steps, this project report identifies and analyzes system constraints to establish a theoretical framework for such a design. Based on data presented in this study, simulations suggest that two $500 \times 500 \text{ um}^2$ stacked CMOS Active Pixel Sensors (APS) with a 500 um separation could be used to localize a tumor with a 300 um radius up to 5mm from the sensor interface.

Contents

Contents	4
Introduction of Variables	6
1. Introduction.....	7
1.1 Novel Cancer Surveillance Technique.....	8
2. Background.....	11
2.1 Relevant Work	11
2.2 Radiolabeling Techniques.....	12
2.2.1 Beta Radiation Energy	13
2.2.2. Beta Energy Loss Through Tissue.....	14
2.3 Optimal Sensing Technique.....	15
2.3.1 APS Signal Generation	17
2.3.2 Stacked CMOS APS Design.....	19
3. Design Methodology.....	21
3.1 Design Objective.....	21
3.2 Design Constraints: Two Main Sources of Error.....	21
4. Background and Tumor Signal Flux.....	24
4.1 Theoretical Model of Flux	24
4.2 Computational Model of Flux.....	28
4.3 Limitations on Number of Pixels and Sampling Rate	31
4.3.1 Minimum Number of Pixels	31
4.3.2 Minimum Sampling Rate.....	32
5. Electrical Noise Analysis.....	33
5.1 Sources of Electrical Noise.....	33
5.2 Probability of Error.....	34
5.2.1 Noise Distribution For No-Event.....	34
5.2.2 Noise Distribution For An Event	35
5.2.3 Probability of Event/No-Event	35
5.2.4 Optimal Threshold:	36
5.3 Limitations on Required SNR.....	37
5.4 Electrical SNR Analysis	38
5.4.1 Output Referred Noise	39
5.4.2 Device Characterization.....	40

6. Discussion of Results	42
7. Conclusion and Future Work	44
Appendix.....	45
References.....	48

Introduction of Variables

3-T	3-Transistor
A/D	Analog to Digital Converter
ADC	Anti-body Drug Conjugate
APS	Active Pixel Sensor
CMOS	Complementary Metal-Oxide Semiconductor
E	Beta Particle Energy
EHP	Electron Hole Pair
k	Number of events/radioactive decays
No	Initial number of ^{32}P Atoms present at the start of decay
NoB	No for healthy (background) cells
NoT	No for tumor cells
PET	Positron Emission Tomography
PN	Joined P-Type to N-Type Semiconductors
PSMA	Prostate-Specific Membrane Antigen
R	Beta particle incidence rate
RB	Background beta particle incidence rate (β/sec)
Rs	Tumor signal incidence rate (β/sec)
S(E)	Stopping Power (Energy Loss) in a medium with E Initial Energy
SBR	Tumor Signal to Background Ratio
SNR	Signal to Noise Ratio (Electronics)
Ts	Sampling Period
WblCDF	Weibull Cumulative Density Function
$W_{\text{depletion}}$	Depletion region width
x	Distance a beta particle travels before hitting the sensor
α	Sensor volume detectable angle
λ	Half life
μ	Gaussian noise distribution mean
$\rho_{\text{background}}$	Background binding density
ρ_{Silicon}	Density of Silicon [g/cm^3]
σ^2	Gaussian noise variance, with standard deviation σ
ϕ_B	Background flux rate

1. Introduction

Cancer is a disease process that develops as a result of genetic and epigenetic alterations within a normal cell. It is known that these malignancies can vary in the rate of growth and progression [1]. Modern cancer surveillance techniques suffer from two major obstacles that prevent localization of initial cancer growth: (i) there is a resolution limit that constitutes the minimum tumor growth required for successful image detection, and (ii) there are no molecular markers to differentiate cancerous tissue from healthy tissue [2]. Using contemporary imaging technology, a tumor must grow to a diameter of at least 1mm before it may be emitted into an image [2,19]. Even if the tumor is large enough for image resolution, the tumor must be identified without the aid of any molecular markers [1,20]. Detection of malignancies is vital to patient treatment, outcome, and survival; therefore, better detection techniques would enable better survival rates [2].

The constraints on current imaging technology prevent doctors from promptly detecting and quickly intervening at the early stages of growth, which may subsequently prevent neoplasm intervention before dissemination [1]. Once a tumor has metastasized and spread to other regions of the body, treatment and detection becomes complicated. Often times, metastatic tumors are the cause of death due to the invasion and domination of malignant cells within the body [2]. Based on the analysis of several clinical cases of metastases and time of dissemination, research studies show that “metastases start to grow years before the ... tumor is clinically detectable” [2-5]. In one particular research study of breast cancer dissemination, Von Fournier et al. concluded that tumors as small as 0.6mm in diameter have the potential to seed distant metastasis [4].

Current imaging technology is done from outside the body. We hypothesize that imaging from within the body would overcome these constraints and would allow for detection of smaller

tumors. Thus, this would enable earlier detection, earlier treatment, and better prognosis for survival of the patient. This project aim will specifically focus on the detection of prostate cancer within the male population. Particular consideration for this tumor was chosen because evidence has shown that locally recurrent prostate tumors have a high potential for metastasis [1].

1.1 Novel Cancer Surveillance Technique

We propose a novel cancer surveillance technique that: (i) resolves um-scale tumor recurrence in the area of primary growth, and (ii) differentiates tumor cells from healthy cells using radiolabeled antibody drug conjugation. *Our objective is to detect locally recurrent cancer before potential dissemination, at 100,000 cells (tumors with a 300um radius). To achieve this, implantable micro-sensors are used in conjunction with antibody molecular markers to assert and localize cancer growth.* The proposed technique is outlined in Figure 1.

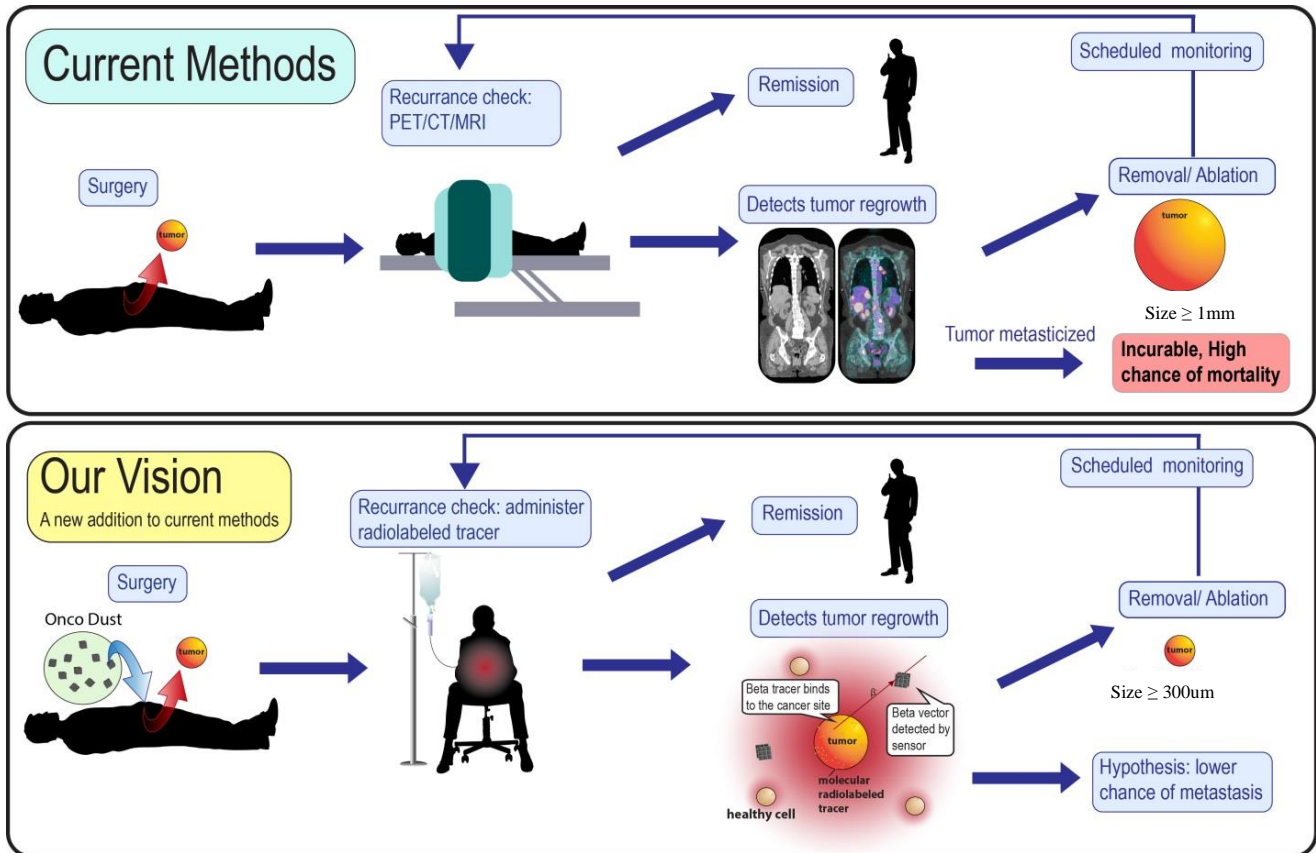


Figure 1: Outline of Novel Cancer Surveillance Procedure In Comparison to Current Methods (Image courtesy of Stefanie Garcia)

To prove feasibility of our novel cancer surveillance technique, prostate cancer is used as a test model (as explained in the introduction) because of the wide availability of clinical data and its significant prevalence among the male population [6]. Our technique could also be extended to breast cancer surveillance in future trials. As outlined in Figure 1, our surveillance method goes as follows:

- 1) After removal of the primary tumor, a network of radiation-detecting micro-sensors is placed within the region of primary growth.
- 2) Every few months, the patient comes to the doctor's office for a screening.

- 2.1) Radiolabeled anti- body drug conjugates (ADC's) are intravenously administered to the patient.
 - 2.2) If there is any cancerous growth within the body, the drug conjugates will bind to the tumor site within 4 hours, and the rest will be washed out. Though most ADC's will bind at the tumor site, there will be some background binding on healthy tissue.
 - 2.3) ADC's are constantly emitting radiation as they undergo radioactive decay. The localized source of radiation will reveal the relative size and location of the tumor.
 - 2.4) Power and communication with the implanted micro-sensor may be accomplished using ultrasonic excitation of piezoelectric transducers, as presented in D. Seo's research publication [5]. Raw sensor readings will be transmitted when powered.
 - 2.5) Sensor data will be externally reconstructed and analyzed. Cancer recurrence, at a specified size and location, can then be assessed.
- 3) If cancer recurrence is detected, targeted radiation treatment, or other cancer therapeutics, could be utilized to remove the tumor and prevent metastases or further growth.

This project report is arranged as followed. Section 2 outlines the foundational constraints on designing a radiation-detecting implantable micro-sensor. Section 3 outlines a refined objective and design methodology for achieving an optimal design. Section 4 analyzes the maximum noise requirements and specifies probability of error. Section 5 analyzes the circuit

architecture and characterizes the pixel sensing circuit. Section 6 summarizes the design results and discusses the implications. Section 7 presents plans for future work.

2. Background

Implantable radiation micro-sensors have not been pursued in the past due to limitations in powering and communicating with such devices, as well as limitations on anti-body drug conjugates.

2.1 Relevant Work

Recently, radiation and oncologist researchers from Washington State University and University of California-San Francisco have developed a “PSMA [Prostate Specific Membrane Antigen] targeted inhibitor for PET imaging of prostate cancer” that achieves high binding rates and enables molecular labeling of cancerous cells [7]. Using inhibitor-based Anti-body Drug Conjugation (ADC), PSMA could be used to identify tumor growth at the cellular level (it is current clinical practice to use PSMA as indicators of prostate cancer cells) [7]. To achieve cellular identification, PET (positron emission tomography) cannot be used, as this imaging technique suffers from the limitations outlined in the introduction. Instead, micro-sensors employed with radiolabeled ADC’s could be used to localize um-scale tumor sites within the body [8]. Radiolabeled ADC’s, which are ADC’s labeled with radionuclides, would exhibit decay as they bind to cancer cells [8]. This radiation could then be detected and localized with nearby micro-sensors.

Based on preliminary data for PSMA targeted inhibitors, radiolabeled ADC's bind to cancerous cells over healthy cells with a specificity of 30:1 [7]. Furthermore, a conservative estimate on the number of bound ADC's over one cancerous cell is about 5000 [7].

In the advancement of micro-sensor wireless power harnessing, implantable neural sensor experiments have shown that “low-power CMOS circuitry coupled with ultrasonic power delivery and backscatter communication” can harness ~500uW with a 1mm² sensor [5]. As proposed in the findings, this power may be scaled with sensor size. These power estimates provide sufficient amounts of energy to excite a low-power CMOS implantable micro-sensor [5].

The previously outlined research efforts support the foundational feasibility of our cancer surveillance method. In the following section, radiolabeled ADC's are characterized to identify fundamental limits on the sensing mechanism and required sensitivity.

Preliminary Data for Implantable Micro-Sensor Design	
Cancer to Healthy Cell ADC Binding Rate	30:1
Number of Bound ADC's Over One Cancer Cell	5000 P-32/cancer cell
Available Power:	500uW/mm ² Sensing Area

Table 2.1 Summary of Preliminary Data Estimates for Implantable Micro-Sensor Design [7]

2.2 Radiolabeling Techniques

Modern cancer therapeutics consist of radiotherapy that uses gamma and alpha radiation for treatment. Since cancer patients will likely have been exposed to both of these types of radiation, only beta emitting radionuclides are considered for radiolabeling ADC's to prevent residual radioactive remnants from affecting the sensor signal.

The ideal beta emitter would be reactive with our PSMA targeted inhibitor and would also emit energies high enough for relatively long distance radiation detection. Beta emitters

compatible with the PSMA targeted inhibitor include ^{32}P , ^{36}Cl , ^{14}C , and ^{35}S . The decay equations and resultant emitted energies of these radionuclides are outlined in Figure 2.1. Of the possible beta emitters, ^{32}P is analyzed in our cancer surveillance model because of its relatively high energy.

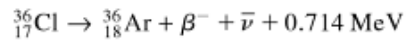
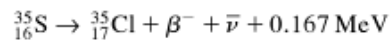
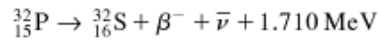
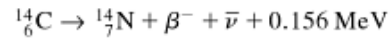


Figure 2.1 Possible Beta Emitters for Radiolabeled PSMA Targeted Anti-body Drug Conjugates

2.2.1 Beta Radiation Energy

^{32}P decay releases 1.71MeV, of which the antineutrino and beta particle (fast moving electron) release as an energy continuum with a distribution shown in Figure 2.2 [9]. The average beta particle energy is 0.56 MeV, and the maximum energy is 1.71MeV [9]. The energy spectrum is approximated using a Weibull distribution with parameters $a = 0.67$ and $b = 2.00$. The fitted distribution is derived in Appendix Section 1.

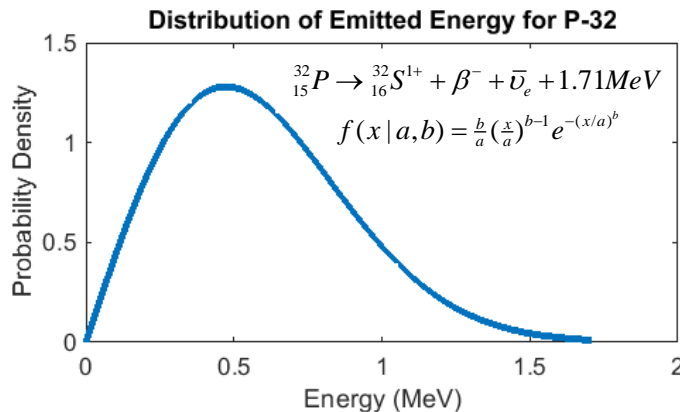


Figure 2.2: Figure 1.4: Beta Electron Energy Distribution During ^{32}P Beta Decay [9]

2.2.2. Beta Energy Loss In Tissue

To detect a signal from a radiolabeled ADC, a beta particle must deposit some amount of energy on the sensor after experiencing energy loss and deflection during its travel through tissue [9]. The causes of energy loss and deflection are briefly outlined in Appendix Section 2. The key point is that stopping power $S(E)$, given in g/cm^2 , models energy loss as it travels through a medium [18]. The stopping power for beta electrons traveling through tissue is shown in Figure 2.3a [18].

Using stopping power, energy loss may be determined. Figure 2.3b outlines energy loss per unit length traveled (x) in tissue based on initial energy. Figure 2.3d outlines the incident energy distribution for beta particles at $x = 5\text{mm}$. A negative energy means that a beta particle at 5mm with the indicated initial energy will not make it to the sensor. Figure 2.3c outlines the percentage of beta particles that travel to a specified distance based on the initial energy distribution and respective stopping power. For this figure, the Weibull Cumulative Density Function (denoted $wblCDF$) approximates the energy distribution. As presented in Figure 2.3c, approximately 15% of emitted beta particles have the potential to travel to 5mm, 7% have the potential to travel 6mm, and 2% have the potential to travel 7mm.

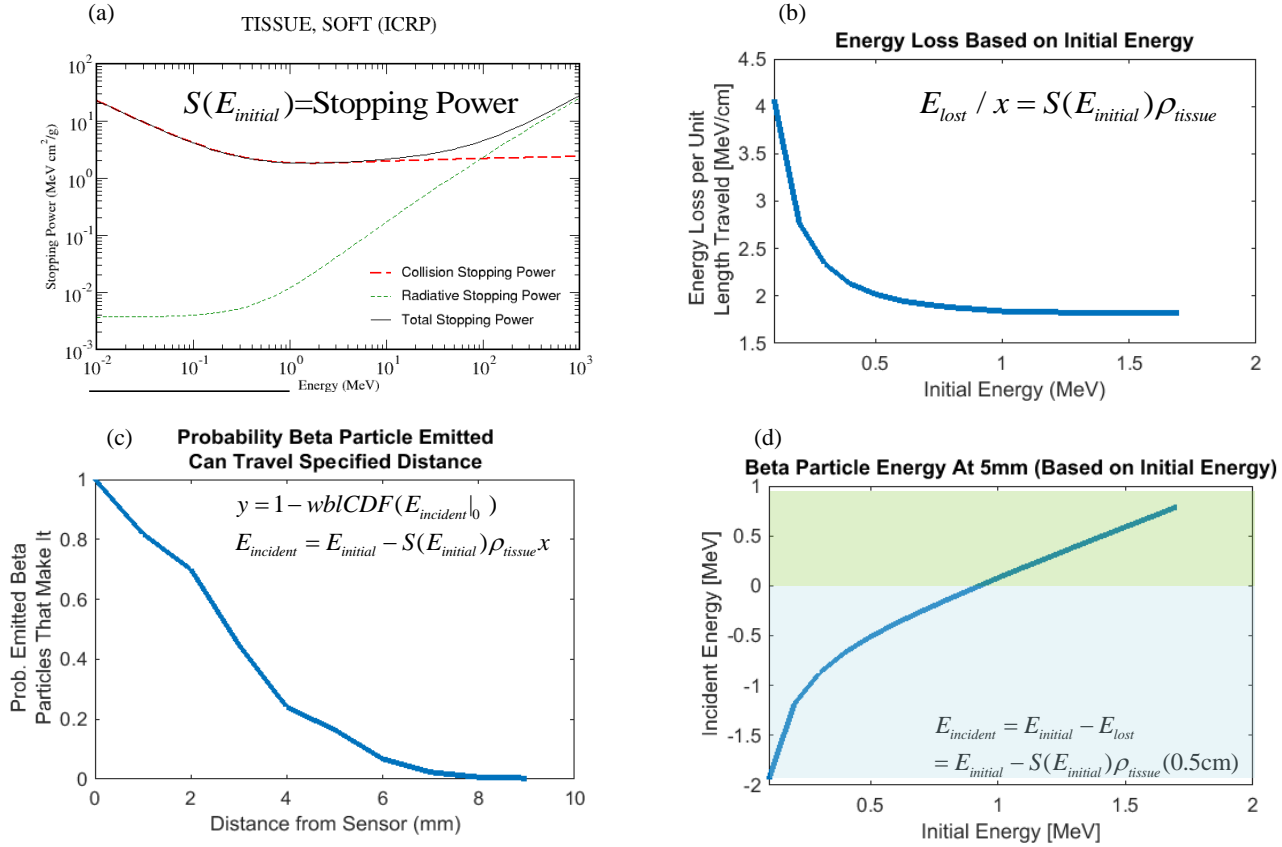


Figure 2.3: (a) Beta Electron Stopping Power through tissue [18] (b) Energy Lost Per Unit Length Traveled Based on Initial Energy (c) Percentage of Beta Particles that Can travel Specified Distance (d) Incident Energy at 5mm Based on Initial Energy [9]

2.3 Optimal Sensing Technique

Given the distribution of energy deposited on the sensor, there are several methods to measure and isolate the beta particle signal. Potential detection methods are outlined in Table 1.2.

The simplest detection method utilizes a PN junction to detect incoming beta particles and measures the current across the diode junction. Due to the low decay rate of ³²P, this method is not feasible since there is not enough charge deposited on the junction to generate detectable amounts of current. Other methods could overcome this limitation by integrating charge over some amount of time and measuring the resultant voltage differential. To accomplish charge

integration, a floating-gate flash memory design or a passive integration sensor could be used; however, the high radiation influx could potentially damage the insulating gate oxide, resulting in a high probability of faulty readings [10,11]. Another charge detection architecture that is less affected by oxide damage is the Active Pixel Sensor. The CMOS Active Pixel Sensor (APS) integrates charge on a small PN junction and induces a voltage on the sensing node [12]. Charge integration (signal generation) is accomplished through the junction capacitance in the depletion region of the PN junction; thus, radiation defects pose no immediate hazards over the sensing area [12].

Measured Variable	Sensing Technique	Description	Findings
Current	PN Junction/ Diode	Current generated from incoming e-; measure current across diode	Doesn't generate enough current. Detecting aA of current is not feasible, electronic noise would dominate
Voltage	Floating Gate Flash Memory	Charge integrated on floating gate; measure voltage on floating gate cap	Too much oxide damage would occur during initial intravenous infusion; would lead to defective sensor readings
Voltage	Passive Integration Sensor	Incoming e- damage HfO2 layer; measure resistance from damaged	Too much HfO2 damage would occur during initial intravenous infusion; would lead to defective sensor readings
Voltage	CMOS Active Pixel Sensor	Charge integrated on diode cap; measure voltage over short timeframe	Feasible to detect spike in charge from a single beta particle if integrated over short timeframe

Table 2.2 Radiation Detection Techniques

Among several studied sensing architectures, the most feasible sensing method, given the limitations of the radioactive decay scenario, is the CMOS APS. Using CMOS APS as sensing elements provides several advantages:

- Using a small PN-junction, it generates a measurable charge-induced voltage change from a single beta particle.
- The sensing element (PN-junction) does not immediately depend on an insulating gate oxide. This design has less gate capacitance area compared to other sensor techniques, making it less susceptible to radiation damage.
- CMOS allows for a mass-producible, cost-effective device fabrication, and also allows a means of providing radiation-protection.

Based on the several limitations posed to the system, CMOS APS is a feasible architecture on which to design a beta radiation sensor for cancer localization.

2.3.1 APS Signal Generation

A typical 3-T CMOS APS circuit is represented in Figure 2.3. The architecture is explained in the figure. Signal is generated and readout in the following manner:

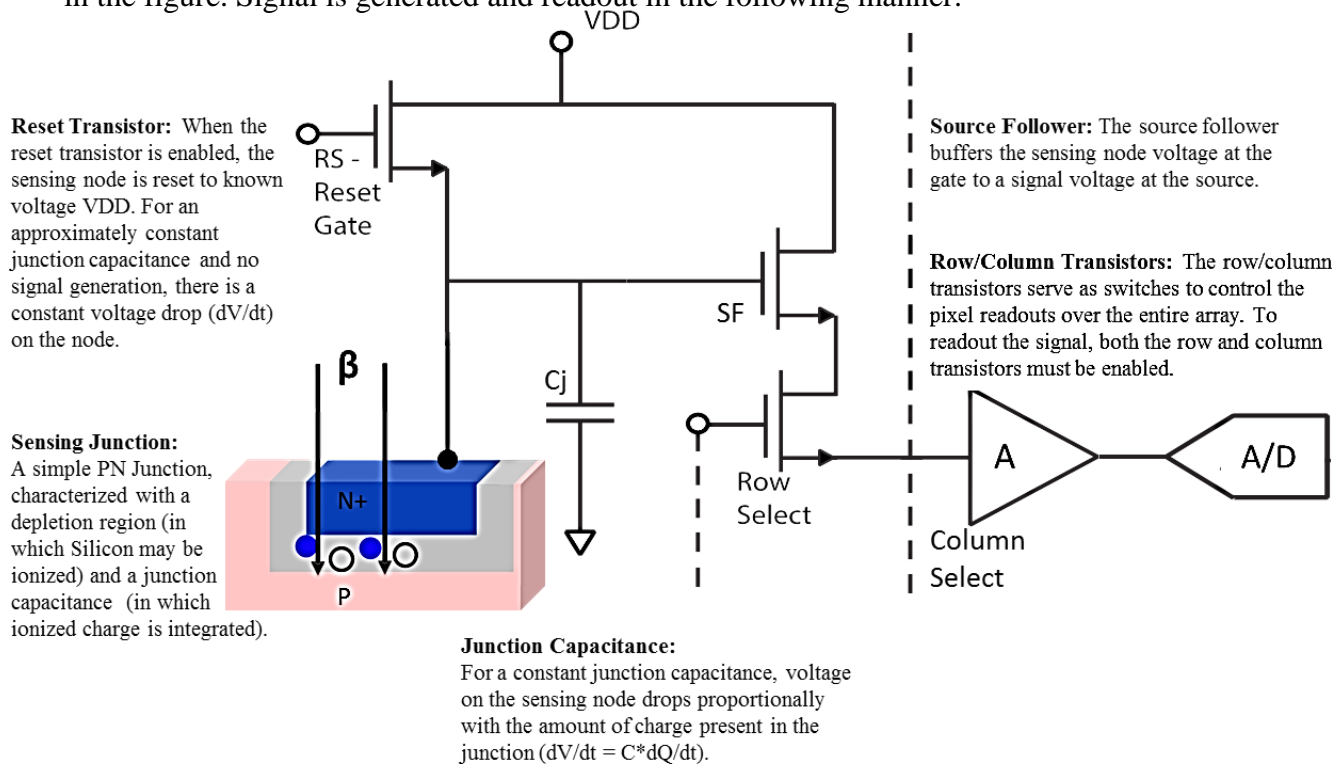


Figure 2.3 3-T CMOS Active Pixel Sensor

1. **Silicon is Ionized:** As beta particles pass through the sensor, they deposit some amount of energy within a pixel PN junction. This energy ionizes silicon (primarily in the depletion region of the sensing junction) and generates Electron Hole Pairs (EHP) within the firing pixel. The firing pixel denotes the individual pixel that experiences an event (was hit with the beta particle).
2. **Signal Converted to Instantaneous Voltage Drop:** Charge generated from EHP's is integrated within the junction capacitance over a short sampling frequency. The increased charge in the junction dQ is reflected through an increased voltage across the junction capacitor ($dV = C*dQ$). When there is no additional charge generation in the sensing junction (no event), the sensing node will experience a constant drop in voltage due to dark current. When energy is deposited (event occurred at the junction), there is an increase in charge in the sensing junction. This charge will induce a larger voltage drop on the sensing node in a single sample (compared to a no-event sample).
3. **Array is Sampled:** The voltage across each pixel in the array is readout by enabling the row and column transistors in a sequential order.
4. **Ultrasonic Backscatter Data Transmission:** After amplification and digitization, the sampled signal is modulated via the piezoelectric crystal and picked up by the external ultrasonic transducer.

As explained in the signal generation mechanism above, energy deposited within the depletion region of the sensing junction generates a measurable charge-induced voltage during one sample. The voltage generated over a short sampling period is outlined in the equations below. Assuming an approximately constant junction capacitance, the signal is directly

proportional to the incident energy. As an example distribution, Figure 2.5 portrays EHP generation based on incident energy for a depletion region width of 1 μ m.

$$E_{deposited} = S(E_{incident})w_{depletion}\rho_{Si}$$

$$EHP = E_{deposited} / E_{ionization,Si}$$

$$dQ = EHP \times q$$

$$dV = QdC + CdQ$$

$$dV \approx CdQ \approx S(E_{incident})w_{depletion}\rho_{Si}q / E_{ionization,Si}$$

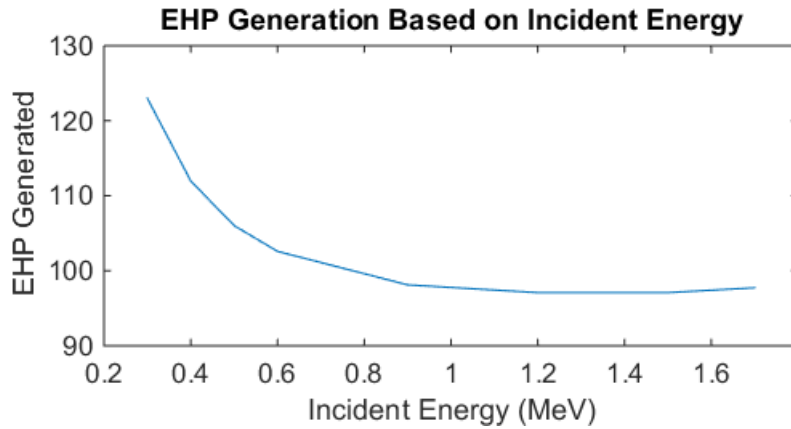


Figure 2.5: (a) EHP Generation Based on Incident Energy

2.3.2 Stacked CMOS APS Design

As previously described, there is a large amount of background radiation present in over our sensor (from ADC bindings to healthy tissue). If a single APS were used, the sensing area would be overwhelmed with background radiation, and there would also be no means of localization. To overcome this constraint, we propose that placing two Active Pixel Sensors back-to-back would allow for tumor signal isolation and localization. A single APS would only detect beta particle events and would have no sense of localization, since background radiation would overwhelm the sensing area and dominate signal readings. Placing two APS back-to-back would allow for localization. Each incoming beta particle would cause a single event on each of the two sensors over the same sample (beta particles travel at high speeds) [9]. Drawing a vector

from the two firing pixels on the sensors would reveal the relative location in which the beta particle originated. Over a large number of samples, a tumor would cause several event vectors to intersect over a small area, effectively suppressing uniform background radiation vectors. Figure 2.6 illustrates this scenario. Figure 2.6a shows how an event vector would be extrapolated. Figure 2.6b shows that an overwhelming number of event vectors originate from the background bindings. Over a large number of samples, the background vectors become uniform and randomly distributed over the sensor area. Using sophisticated noise suppression techniques, the uniform noise could be subtracted to isolate the tumor signal. 2.6c shows event vectors that would originate from a tumor without the presence of background.

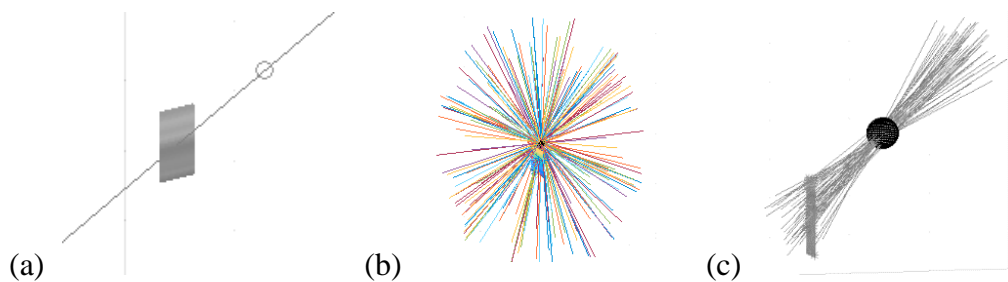


Figure 2.6: Vectors from (a) Single Event (b) Background Events (c) Tumor Events

3. Design Methodology

For an optimal sensor design, each design constraint must be carefully weighed to maximize tumor signal localization and minimize noise and background radiation.

Table 2.1 outlines the foundational design constraints of the entire system. As presented in Section 1.1, the primary objective of this project report is to design an implantable CMOS Active Pixel Sensor that, in conjunction ^{32}P Radiolabeled Anti-body Drug Conjugates can detect locally recurrent tumors with a minimum 300um radius. Based on the background analysis made in Section 2, the objective is further refined in the following section.

3.1 Design Objective

As presented in Figure 2.3d, 15% of emitted beta particles have the potential to travel to 5mm. Since most of the beta particles from 5mm-7mm in front of the sensor will not have enough energy to make it to the sensor, only a 5mm detection sphere will be considered in this design. Background analysis on relevant work led us to an objective refinement: *our objective is to design a CMOS APS that can detect tumors with a 300um radius at a maximum of 5mm from the sensor with minimum 98% confidence.*

3.2 Design Constraints: Two Main Sources of Error

There are two inherent sources of error that constrain our design objective: (1) background ADCs that bind to healthy tissues and drown the tumor signal, and (2) electrical noise that may cause fluctuations in the sensor readings. SNR and SBR are terms used to differentiate the two sources of error:

- $SBR = \text{Signal to Background Ratio} = \frac{\text{Beta Particles From Tumor Signal}}{\text{Beta Particles From Background}}$

SBR is the ratio of the tumor signal flux versus background flux, where flux denotes the expected number of incident beta particles over the sensor per second. Tumor Signal refers to the signal of interest (those beta particles originating from the tumor). Background flux refers to those beta particles (ADCs) that bind to healthy tissue.

- $SNR = \text{Signal to Noise Ratio} = \frac{\text{Electrical Signal Energy}}{\text{Electrical Noise Energy}}$

SNR refers to parameters in the electrical domain and represents the ratio of signal energy (E_s) to noise spectral density (N_o) for the sensor circuit. For an APS, signal energy represents the amount of charge-induced voltage generated in the PN junction from an event, and noise spectral density is derived from the equivalent input referred electrical noise from the system.

Both SBR and SNR impose significant design constraints that affect different design parameters. Our design is based on the careful analysis of both constraints. Figure 3.1 outlines the design methodology for achieving the refined objective of Section 3.1.

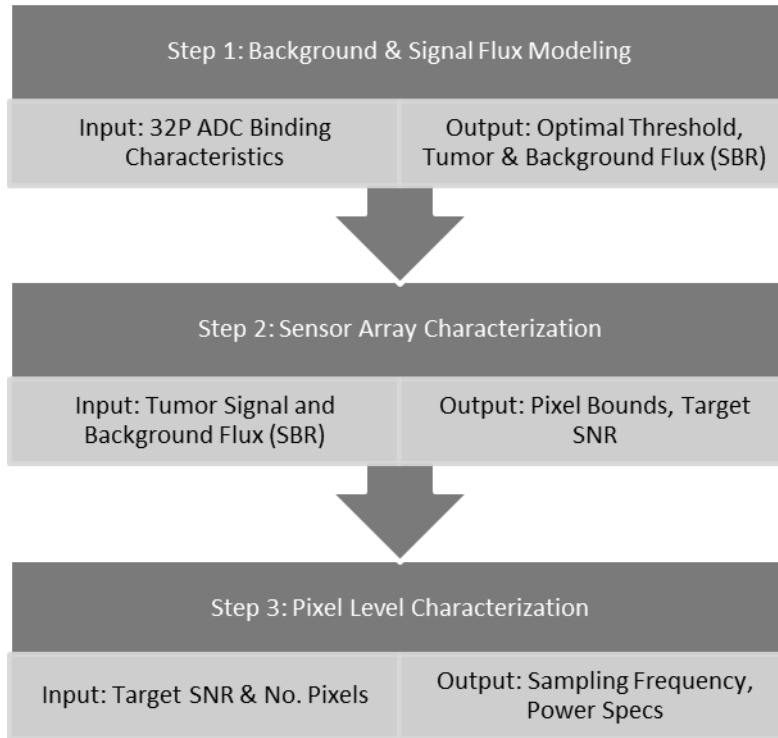


Figure 3.1: CMOS APS Design Methodology

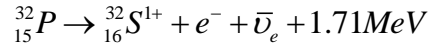
This design methodology is followed in the following two sections. Section 4 analyzes the tumor signal to background ratio (SBR) through derivation of the tumor and background beta particle flux. Section 5 analyzes the electrical signal to noise ratio (SNR) of the pixel array circuit and derives the minimum detectable signal and probability of error.

4. Background and Tumor Signal Flux

Sources of error arising from background bindings cause the sensor to output false positives. This is an inherent limitation of our system dictated by our radiolabeled inhibitor-based ADC. As explained in Section 2.1, the radiolabeled ADC binds to tumor and healthy cells with a specificity estimate of 30:1 [7]. This means, that to successfully detect a tumor at 5mm, the sensor would have to isolate the tumor signal from background bindings. The scenario is analyzed in the following sections.

4.1 Theoretical Model of Flux

The beta particle flux may be estimated from the decay equation. The beta decay equation for ^{32}P is given by:



$$\beta = N_0 e^{-\lambda t}$$

$$\frac{d\beta}{dt} = N_0 \lambda e^{-\lambda t}$$

$$\lambda = \frac{\log 2}{14.3\text{days}} = \frac{\log 2}{1.2E6\text{sec}}$$

No is the initial amount of radioactive atoms present at the start of decay, and λ is the half-life of ^{32}P [9]. With the specified ^{32}P PSMA ADC, the molecular probes would settle within the body about 4 hours after initial intravenous injection [7]. The beta decay rate at 4 hours is approximately equal to the initial decay rate.

$$\frac{d\beta_{4\text{hrs}}}{dt} = N_0 \lambda e^{-\lambda 4\text{hrs}} = N_0 \lambda (0.99)$$

$$\frac{d\beta_{0\text{hrs}}}{dt} \simeq \frac{d\beta_{4\text{hrs}}}{dt} = N_0 \lambda$$

As outlined in Table 2.1, there is ~5000 bound ADC's on a single tumor cell, and due to the background binding ratio of 30:1, there are ~5000/30 bound ADC's on a healthy cell. For a tumor with a 300 um radius, assuming a spherical shape, the tumor volume is ~ 110E6 um³ and consists of ~110E3 tumor cells (1 cell = 1000 um³) [13,14]. With 5000 β/cell, the initial number of radioactive atoms present over the tumorbed is:

$$N_{OT} = 5000 * 110E3 = 550E6$$

The tumor flux will radiate spherically from the point source and decreases by 1/x² as the distance from the source increases.

$$\Phi = \text{Radiative Flux } (\beta/\text{sec}/\text{um}^2)$$

$$\Phi = \frac{d\beta}{dt} \frac{1}{4\pi x^2} = \frac{N_0 \lambda e^{-\lambda t}}{4\pi x^2}$$

$$R = \text{Incidence Rate } (\beta/\text{sec})$$

$$R = \Phi A_{\text{Sensor}} = \frac{N_0 \lambda e^{-\lambda t} A_{\text{Sensor}}}{4\pi x^2}$$

The beta particle incident rate R on the sensor is defined as the amount of radiative flux over the sensor surface area. The expected beta particle incidence rate for tumors of various radii and various distances from the sensor is outlined in Table 4.1.

Tumor Incidence Rate (β/sec), 500x500um² Sensor

	R=200um	R=300um	R=400um	R=500um
D=1mm	149	504	1196	2337
D=2mm	32	110	261	511
D=3mm	8	28	66	129
D=4mm	3	11	26	51
D=5mm	1	3	8	16

Table 4.1a: Tumor Incidence Rate (β/sec) over a 500x500um² sensor for various tumor sizes and distances

Tumor Incidence Rate (β /sec) over a 1x1mm² Sensor

	R=200um	R=300um	R=400um	R=500um
D=1mm	598	2019	4787	9350
D=2mm	130	441	1047	2045
D=3mm	33	112	265	519
D=4mm	13	44	104	204
D=5mm	4	14	33	65

Table 4.1b: Tumor Incidence Rate (β /sec) over a 1x1mm² sensor for various tumor sizes and distances

To determine the total contribution of background radiative flux incident on the sensor, the background binding density must be integrated over the entire detectable volume (spanning some angle and distance). The background binding is 5000/30 β /healthy cell. With an approximate cell size of 1000 μm^3 , the background binding density is

$$\rho_{Background} = \frac{5000}{30} \frac{1}{1000} \approx .017 \left[\frac{\beta}{\mu\text{m}^3} \right]$$

The detectable distance from the sensor is 0 – 7mm, as was presented in Figure 2.3d. The detectable azimuthal and polar angle depends on the separation between the two sensors as well as the sensor size. For separation S and sensor length L , the azimuthal detectable angle α is given by the equation below. If the sensor has the same length along the other edge (it's a square), the polar detectable angle would be the same as the azimuthal detectable angle.

$$\alpha = 2 \tan^{-1}(L / S)$$

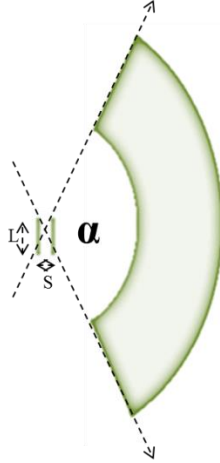


Figure 4.1: Determining the Azimuthal and Polar Detection Angles

Using spherical coordinates, the total detectable volume of the sensor may be approximated by taking the volume integral from 0 – 7mm (detectable distance) over α (the detectable azimuthal and polar angle). To get the total number of background beta particles No_B present, the background binding density is multiplied with the total detectable volume. No_B , combined with λ , yields the total number of background beta particles emitted in that volume per unit time $d\beta/dt$. The background incidence rate is then found by incorporating the $1/x^2$ flux decrease.

$$\frac{d\beta}{dt} = 2\lambda \int_{x=0}^{7mm} \int_{\theta=\pi/2-\alpha}^{\pi/2+\alpha} \int_{\phi=\pi-\alpha}^{\pi+\alpha} \rho_{Background} x^2 \sin \theta \, dx d\phi d\theta$$

$$R_{background} = \frac{d\beta}{dt} \frac{1}{4\pi x^2} = \frac{\lambda \rho_{Background}}{2\pi} \int_{x=0}^{7mm} \int_{\theta=\pi/2-\alpha}^{\pi/2+\alpha} \int_{\phi=\pi-\alpha}^{\pi+\alpha} \sin \theta \, dx d\phi d\theta$$

This approach slightly underestimates the amount of background radiation present since the detectable volume is not entirely spherical. This approach serves as model to yield a rough estimate on the expected background incidence rate. Monte Carlo simulations, outlined in the following section, validate the relative accuracy of these results.

Correcting for the energies and range (from Figure 2.3d), the mean probability that a beta particle from 0 – 7m will hit the sensor based on the energy distribution is ~40%. The estimated background flux for various sensor sizes are listed in Table 4.2. Increasing the sensing area increases the amount of background radiation detected by the sensor, while decreasing the separation increases the detectable volume and also increases the detected background radiation. For a 500 x 500 μm^2 sensor with a separation of 500 μm , $R_B \cong 600 \beta/\text{sec}$.

	L [μm]	S [μm]	α [rad]	Rbackground (β/sec)	Incorporating Energy Loss
Varying Length	100 μm	500 μm	1.4	5	0
	500μm	500μm	0.8	1700	595
	1mm	500 μm	0.5	14000	5600
Varying Sep	500 μm	100 μm	0.2	4900	1715
	500 μm	500 μm	0.8	1700	595
	500 μm	1mm	1.1	750	260

Table 4.2: Estimated Background Incidence Rates for Various Sensor Sizes and Separations

4.2 Computational Model of Flux

A Monte Carlo approach was taken in order to simulate the behavior of an incoming beta particle over the sensor. Figure 4.3 outlines the procedure.

To run the simulation, the following variables must be chosen: tumor size, maximum beta particle range, sensor size, and sensor separation. From the tumor size and maximum beta particle range, the outward flux of tumor and background beta particles ($d\beta/dt$) is identified. With a fixed simulation time, the number of beta particles originating from the tumor volume and background detectable volume is determined.

After identifying the number of beta particles to generate, the simulation proceeds as follows. For each beta particle, a random originating location is assigned. The location is taken

from a uniform distribution over the respective volume. For particles originating from the tumor, a random point within the tumor volume is chosen. For particles originating from the background, a random point with the detectable volume is chosen. A random direction and random energy is then assigned. The direction is taken from a uniform distribution over all directions (360 degrees by 180 degrees in spherical coordinates). The energy is taken from the fitted Weibull energy distribution of the ^{32}P beta emitters (outlined in section 1 and elaborated in Appendix Section 1).

The random location, direction, and energy constitute one ray which represents the beta particle. For each ray, it is then determined whether or not the beta particle hits the sensor. There are two criteria for hitting the sensor: (i) is the ray traveling in the right direction and does it hit both sensors, and (ii) does the ray have enough energy to make it to the sensor. If the ray satisfies both criteria and makes it to the sensor, the incident energy is used to determine the EHP which would be generated.

The results from the simulation yield the background signal flux, the tumor signal flux, and the amount of charge generated on each sensor from the incident rays. Over a large number of simulations, an approximation of the background signal flux and the tumor signal flux is determined.

Results from the Monte Carlo simulation are succinctly outlined in Table 4.3. As expected, the theoretical model in section 4.1 slightly underestimated the background incidence rate. The calculated R_B from section 4.1 was 600 β/sec , and the simulated R_B from the Monte Carlo results was approximately 650 β/sec , within 10% of the theoretical result. The model also underestimated the tumor signal rate, especially for close distances. This is most probably due to discrepancies in the incident energy distribution approximations.

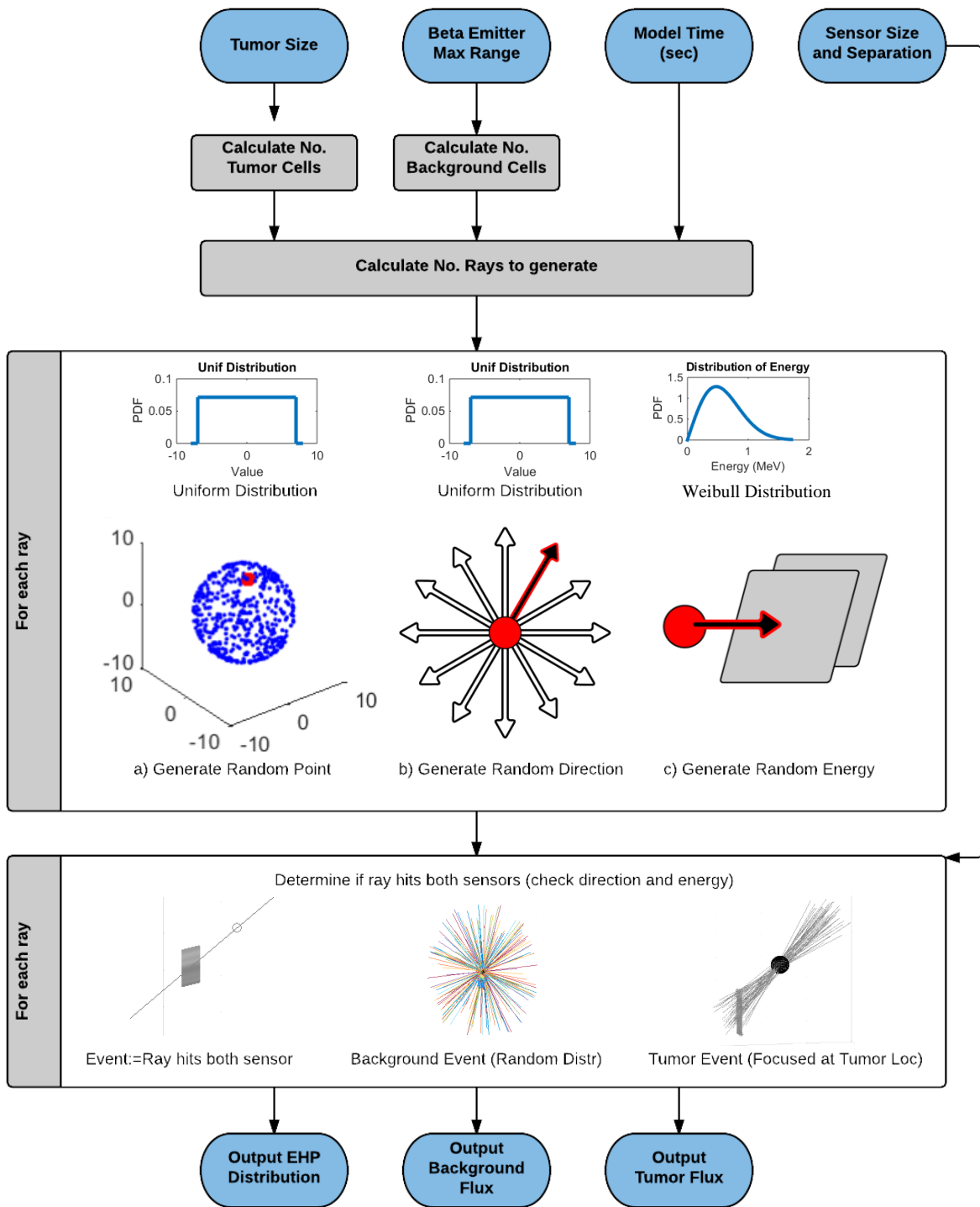


Figure 4.3: Monte Carlo Procedure

	R=200um		R=300um		R=400um	
	Rsig	RB	Rsig	RB	Rsig	RB
D=1mm	88	680	272	688	616	620
D=3mm	3	648	26	628	46	654
D=5mm	0	608	2	648	8	666
Avg RB:					649	

Table 4.3: Monte Carlo Simulation Results

It is important to note that, although this particular Monte Carlo simulation result for a tumor with a 200um radius at 5mm showed an R_{sig} of 0 β /sec, had I ran more simulations, we could expect that, on average, R_{sig} would be 1 β /sec. This expected result is used in the following sections.

4.3 Limitations on Number of Pixels and Sampling Rate

Based on the results from the previous section, the constraints on the minimum number of pixels and minimum sampling rate are defined.

4.3.1 Minimum Number of Pixels

The minimum number of pixels is given by:

$$N_{Pixel} > SBR \frac{R_{Background}}{R_{Desired}}$$

With the background and tumor signal rates outlines in Table 4.3 (Monte Carlo Results), a target design SBR of 10 requires the minimum number of pixels in Table 4.4 to isolate and localize the tumor signal. Since the sensor size is fixed, the number of pixels determines the pixel size. For 4000 pixels, each pixel would be 8 x 8 μm^2 .

	R=200um	R=300um	R=400um
D=1mm	78	26	10
D=3mm	2160	242	142
D=5mm	6080	3240	833

Table 4.4: Minimum Number of Pixels Required for Various Tumor Sizes

4.3.2 Minimum Sampling Rate

Each pixel should be sampled fast enough to only capture a single event during the sampling window. The sampling period should be faster than R_B so that, on average, there is less than one event expected over the sensor over a given sampling period, otherwise successive events would be indistinguishable from one another. Based on the simulation results, the sampling frequency must be much greater than 650Hz.

$$f_s = 1 / T_s$$

$$f_s \gg R_{Background}$$

5. Electrical Noise Analysis

This section focuses on CMOS pixel circuit design. Electrical noise is analyzed, and in particular, thresholds are identified for number of pixels and SNR.

5.1 Sources of Electrical Noise

Parasitics, thermal variations, and effects of other random processes must be kept to a minimum to reduce noise fluctuations in the signal. CMOS noise is largely random, and over a large number of samples, CMOS noise may be characterized using a Gaussian distribution with mean μ and variance σ^2 :

$$f(x) = \frac{1}{\sqrt{2\pi\sigma^2}} e^{-\frac{(x-\mu)^2}{2\sigma^2}}$$

$f(x=a)$ is the probability density of CMOS noise at a . Integrating over values of x , the probability that the noise will be less than a certain value may be estimated using the cumulative density function given by:

$$F(x) = \int_{-\infty}^x f(a)da = \frac{1}{\sqrt{2\pi\sigma^2}} \int_{-\infty}^x e^{-\frac{(m-\mu)^2}{2\sigma^2}} dm$$

The cumulative density function of a Gaussian random variable is best evaluated in terms of the Q function, which cleanly represents information of interest for Gaussian noise.

$$Q(z) = \frac{1}{\sqrt{2\pi}} \int_z^{\infty} e^{-\frac{y^2}{2}} dy \quad \text{where } y = \frac{x-\mu}{\sigma}$$

$$F(x) = 1 - Q\left(\frac{x-\mu}{\sigma}\right) = 1 - 0.5\text{erfc}\left(\frac{x-\mu}{\sqrt{2}\sigma}\right)$$

5.2 Probability of Error

The probability of pixel error is composed of the probability of false positives (detection of a pixel event through the sensing junction when no event has occurred) and the probability of false negatives (failure to detect an event through the sensing junction when an event has occurred). False positives arise from electrical noise, and false negatives arise when a beta particle does not have enough energy to generate a measurable charge-induced voltage.

5.2.1 Noise Distribution For No-Event

The voltage signal that represents that no event has occurred is assumed to be 0V. As outlined in section 5.1, the distribution of noise around the no-event voltage is approximated with a Gaussian function with 0 mean and noise variance σ^2 . Figure 5.1 shows the expected noise distribution. Noise variance is calculated in section 5.4 and is approximated to be 200uV in this analysis.

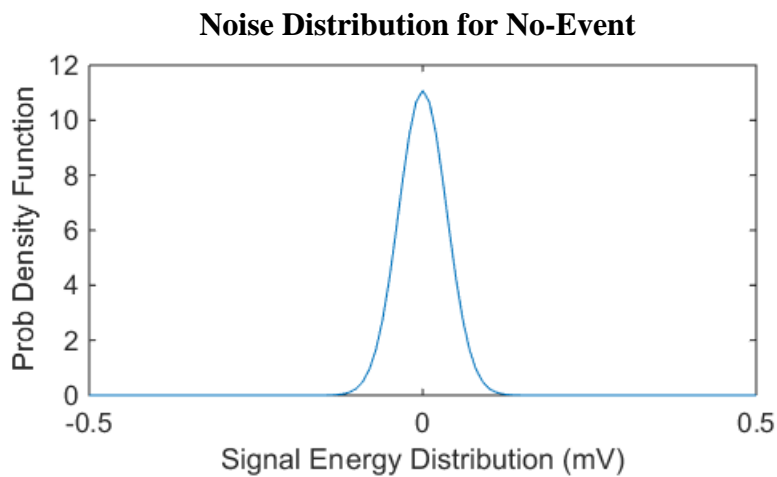


Figure 5.1 Gaussian Distribution of Electrical Noise

5.2.2 Noise Distribution For An Event

When an event is detected by the sensor, not all events will generate the same amount of charge. Some events will hit the sensor with low amounts of energy, and few events will hit the sensor with high amounts of energy. The deposited energy will generate a charge-induced voltage on the sensing node, with the expected mean signal voltage for an event approximated as 2mV (explained in Section 2.3.1). The distribution of expected voltage generation on the sensing node is shown in Figure 5.2.

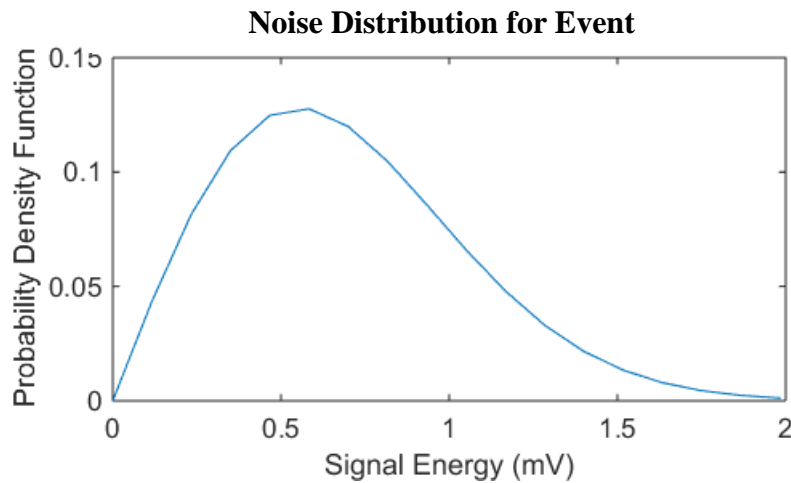


Figure 5.2: Energy Distribution of Incoming Beta Particles.

5.2.3 Probability of Event/Non-Event

The probability of k events occurring (probability of k radioactive decays) is given by a Poisson distribution with mean λ . The expected number of events over a sampling period T_s is determined by the total β incidence flux, which is approximately equal to the background flux rate ϕ_B .

$$f(k, \lambda) = \frac{\lambda^k e^{-\lambda}}{k!} \quad \text{where} \quad \lambda = \Phi_B T_s$$

Assuming that sampling frequency is at least 10 times faster than the background flux rate (as explained in Section 4.3), λ would be 0.1 and the probability of an event and no-event could be approximated as:

$$f(k = 0, \lambda = 0.1) = e^{-0.1} = 0.90$$

$$f(k = 1, \lambda = 0.1) = 0.1e^{-0.1} = 0.09$$

90% of the time there is no event over the sensor, and 9% of the time there is 1 event. 1% of the time there is more than one event over the sensor.

5.2.4 Optimal Threshold:

The optimal threshold would minimize the overall probability of error by minimizing the probability of false positives and probability of false negatives.

$$P(\text{error}) = P(\text{falsePositive}) + P(\text{falseNegative})$$

$$P(\text{falsePositive}) = P(x > \gamma) = 1 - F(\gamma) = Q\left(\frac{\gamma - \mu}{\sigma}\right) = 0.5\text{erfc}\left(\frac{\gamma - \mu}{\sqrt{2}\sigma}\right)$$

$$P(\text{falseNegative}) = P(y < \gamma) = \text{wblCDF}(\gamma) = \int_0^\gamma \frac{b}{a} \left(\frac{y}{a}\right)^{b-1} e^{-(y/a)^b} dy$$

The optimal threshold is presented in Figure 5.3 and is approximately 0.12mV. Since $P(\text{non-event}) = 90\%$ and $P(\text{event}) = 10\%$, the overall threshold is closer to non-event voltage. Figure 5.3b zooms in on the area of interest to illustrate the probability of error. The orange shaded region represents the probability of a false negative, which integrating over the area was found to be 0.3%. The blue region on the right represents the probability of a false positive, which was found to be 0.04%. The total probability of error for the considered case is 0.34%, with a higher probability of false negatives than false positives.

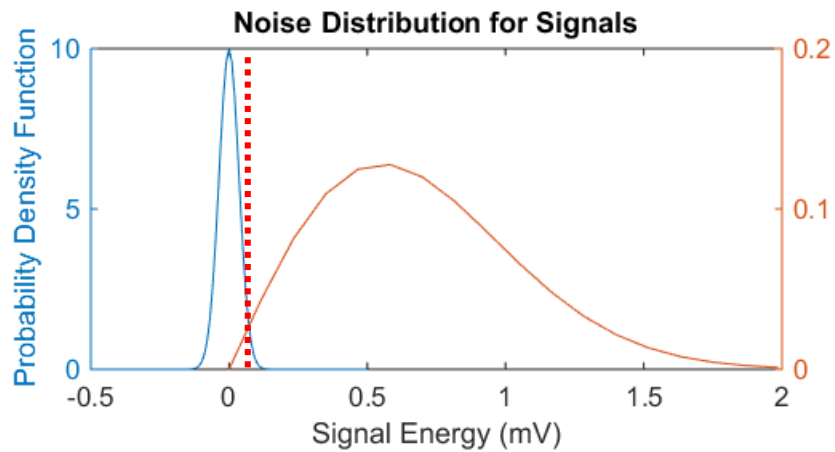


Figure 5.3: Distribution of Noise About Both Signals

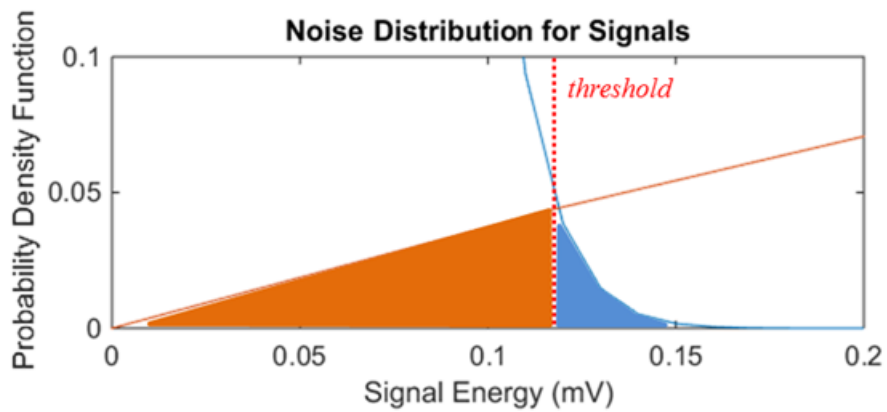


Figure 5.3b: Zoomed in Area of 5.3 Showing Optimal Threshold and Error

5.3 Limitations on Required SNR

The pixel error ratio (PER), which is given by the ratio of pixel errors to total pixels in a given sample period, can be approximated with the pixel error probability $P(\text{error})$.

$$PER \approx P(\text{error})$$

$$PER \approx 1 - F(\gamma) + wblCDF(\gamma)$$

One of the major system constraints is that only one pixel event may occur over a given sample period over the entire array, otherwise events will be indistinguishable from each other and directionality may not be determined. On average, the false pixel rate of one pixel over a sampling period should be less than 1 in order to minimize this error, thus

$$N_{Pixel} PER \ll 1$$

$$N_{Pixel} (1 - F(\gamma) + wblCDF(\gamma)) \ll 1$$

$$N_{Pixel} (0.5 \operatorname{erfc}(SNR) + wblCDF(\gamma)) \ll 1$$

This pixel bound is also taken into consideration with the pixel bound of section 4.3.1. As the number of pixels increases, noise worsens thus SNR decreases. A balance must be achieved between the N_{pix} and SNR to stay within the above constraint.

5.4 Electrical SNR Analysis

In a 3-T CMOS APS, such as the circuit outlined in Figure 2.3, noise in the sensing junction, transistors, amplifier, and A/D converter all negatively affect the signal of interest. The primary and dominating sources of noise in these components are thermal noise, shot noise, and flicker noise [16]. Thermal (Johnson-Nyquist) noise is attributed to random thermal motion of charge carriers within a semiconductor [16]. Shot noise arises from the flow of electrons within a PN junction [16]. Flicker (1/f) noise is also observed in transistors and is known to fall off steadily at higher frequencies [16]. The noise powers (or noise variances) from each of these sources is outlined below.

$$\text{Thermal Noise} \quad v_{n,thermal}^2 = 4k_B TR \Delta f$$

$$\text{Shot Noise} \quad i_{n,shot}^2 = 2qI_{Dark} \Delta f$$

$$\text{Flicker Noise} \quad v_{n,flicker}^2 \approx k_F / WLC_{ox} \Delta f$$

The noise power of the pixel circuit is approximated in the following section in order to determine the minimum detectable signal, optimal sampling frequency, and power requirements.

5.4.1 Output Referred Noise

The sensing junction experiences different amounts of noise under the 2 different modes of operation, during reset (when the reset transistor enabled) and during readout (when the reset transistor is disabled and the source follower transistor is enabled).

During Reset, thermal noise is experienced in the sensing capacitance as:

$$v_{n,reset}^2 = \frac{k_B T}{2C_{pd}}$$

Based on theoretical and experimental analysis of APS reset noise in [15], the expected mean square noise voltage during reset is about 1/2 the expected kT/C value due to short reset times relative to the thermal time (time to charge the junction capacitance to kT/q) [15].

During Readout, thermal, shot, and flicker noise from the junction, transistors, and amplifier are all observed. The noise from each of the sources is characterized by the following:

Junction Noise $v_{n,pd}^2 = 2qI_{Dark}t_{int} / C_{pd}^2 \Delta f$

Source Follower Noise $v_{n,thermal}^2 = 4k_B TR \Delta f$, where $R=2/3g_{m,sf}$

$$v_{n,flicker}^2 \simeq k_F / WLC_{ox} \Delta f$$

$$v_{n,SF}^2 = v_{n,thermal}^2 + v_{n,flicker}^2$$

Amplifier Noise $v_{n,thermal}^2 = 4k_B TR \Delta f$, where $R=2/3G_{m,amp}$

$$v_{n,flicker}^2 \simeq k_F / WLC_{ox} \Delta f_A$$

$$v_{n,amp}^2 = v_{n,thermal}^2 + v_{n,flicker}^2$$

System Noise $v_{n,outputAmp}^2 = A_{amp}^2 (A_{SF}^2 (v_{n,pd}^2 + v_{nSF}^2) + v_{namp}^2)$

Δf for the source follower is the sampling frequency of one pixel ($f_s \cdot \pi/2$), and Δf_A for the amplifier is the array sampling frequency (which is N_{pix} times the sampling frequency of one pixel). Analyzing the noise during readout, the noise is compared to the signal voltage (calculated in Section 2.3.1), and the Signal to Noise Ratio is given by:

$$SNR = v_{\beta_{sig}}^2 / v_{n,total}^2$$

$$SNR_{dB} = 10 \log(v_{\beta_{sig}}^2 / v_{n,total}^2)$$

5.4.2 Device Characterization

To analyze the SNR, nominal values for process parameters are used. The assumed values for this analysis are outlined in Table 5.1.

T	310 [K]	<i>Temperature Inside the Body</i>
kB	1.38E-23[J/K]	<i>Boltzman's Constant</i>
q	1.6E-19[C]	<i>Charge of an electron</i>
Kf	3E-24 [V ² -F]	<i>Flicker Noise Process Parameter [16]</i>
Cpd	0.1 [fF/um ²]	<i>Photodiode Capacitance</i>
IDark	50 [aA]	<i>PhotoDiode Dark Current</i>
Cox	5 [fF/um ²]	<i>Oxide Capacitance</i>
W	10 [um]	<i>CMOS Device Width</i>
L	1 [um]	<i>CMOS Device Length</i>
chm	0.02 [1/V]	<i>Channel Length Modulation</i>
td	1 [um]	<i>Depletion Region Width</i>
S(Einc)	2E6 [eVcm ² /g]	<i>Electron Stopping Power in Silicon [18]</i>
Eion	3.6 [eV]	<i>Ionization Energy in Silicon</i>

Power 100 [uW] *Power Availability*

Table 5.1: Estimated CMOS Process Parameters

Based on these parameters, and a power limit of 100uW, an expected SNR plot of our pixel sensor is shown in Figure 5.4. For this particular design, the minimum number of pixels necessary to detect a tumor at 5mm was ~3200, thus 4000 pixels were considered based on the limits outlined in Section 4.2 and 5.3. Peak SNR is achieved at 300Hz, which based on our minimum sampling frequency limitation presented in Section 4.2 is not possible for this system. At about 10 times the minimum rate (at 6 kHz), the SNR is 50dB, and continues to decline steadily with increasing frequency. In consideration of power limitations and background radiation suppression, 6 kHz would be a feasible sampling frequency because it is fast enough to suppress background events and slow enough to accommodate a large pixel array. With half the amount of power, at 50uW, the SNR at 6kHz is 40dB.

With these design parameters, the charge-induced signal voltage $dV_{\beta sig}$ (introduced in Section 4) may be calculated as:

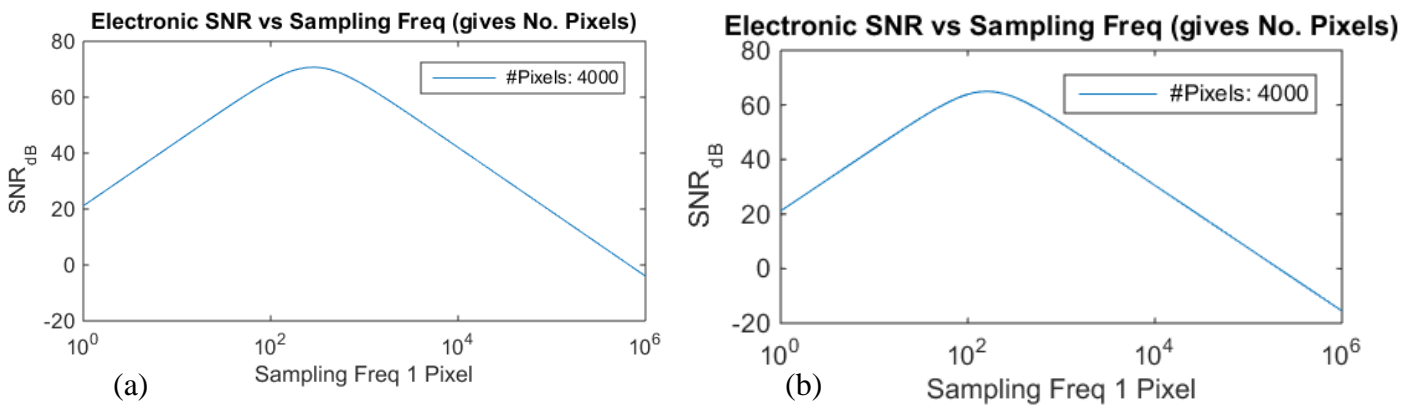


Figure 5.4: SNR Plots (a) 100uW (b) 10uW

$$\begin{aligned}
EHP_{\beta} &= S(E_{inc}) \rho_{Si} t_{depletion} / E_{ion} \\
dQ_{\beta} &= q \times EHP_{\beta} \\
dV_{\beta Sig} &= dQ_{\beta} / (C_{pd} + C_{ox}) \\
dV_{\beta Sig} &= 1.8mV
\end{aligned}$$

The noise variance of our system is modeled by $v_{n,output}^2$, and the minimum detectable signal is the energy of that noise evaluated with our design parameters.

$$\begin{aligned}
v_{n,outputAmp}^2 &= A_{amp}^2 (A_{SF}^2 (v_{n,pd}^2 + v_{nSF}^2) + v_{namp}^2) \\
v_{n,outputAmp} &\approx 0.17mV
\end{aligned}$$

If more time had allowed, we would want to refine several design parameters, such as the amplifier design and A/D converter. Optimal designs of these parameters would minimize the overall noise and could improve the noise sensitivity.

6. Discussion of Results

Based on the theoretical analysis and simulation of background radiation circuit noise, an ideal APS design that can successfully detect and localize tumors with a radius of 300 um has been realized. Our analytical approach shows that a 500 x 500 um² sensor with a separation of 500um will achieve our objective.

In Section 4, the tumor signal and background radiation flux was modeled theoretically and computationally. These simulations showed that a 500 x 500 um² sensor with a 500 um separation could expect a background incidence rate RB of ~650 β/sec. The expected tumor signal at 5mm (emitted from a tumor with a 300um radius) that must be isolated would be ~2 β/sec. These rates set a limit on the minimum number of pixels and the minimum sampling frequency, as explored in Section 4.3. For our objective design, greater than 3200 pixels (57 x 57

pixel array) must be sampled at a frequency greater than 650Hz to isolate the tumor signal. This yields $\sim 9 \times 9 \text{ um}^2$ pixel size, which is well within modern CMOS process limitations.

In Section 5, circuit noise was analyzed to determine if, given the ultrasonic power harnessing constraints, a beta particle could generate the minimum detectable signal with a low enough probability of error. For a standard modern CMOS APS array of 4000 pixels, the minimum detectable signal was identified to be approximately 0.2mV. 6kHz was evaluated as an optimal sampling frequency, as it was well within the limits. At this frequency, the probability of error given the design parameters is $\sim 0.3\%$.

7. Conclusion and Future Work

This initial sensor design analysis presented in this project report proves the feasibility of using a stacked CMOS APS design for cancer surveillance of um-scale tumors. This project report serves as a foundational introduction to the several constraints imposed on implantable radiation-detecting micro-sensors, and also serves as a basis on which a cancer surveillance CMOS Active Pixel Sensor may be designed.

Future work for this project includes modeling the active pixel sensor in Cadence and expanding on the readout circuit, which was not focused on in this project report. The readout circuit would further introduce noise to the system, but a similar analysis could be made to balance conflicting system constraints. Once a circuit design has been validated in Cadence, testing an actual device would yield the most insight on this novel cancer surveillance technique.

Appendix

1. Comparison of Beta Energy Distribution Curves

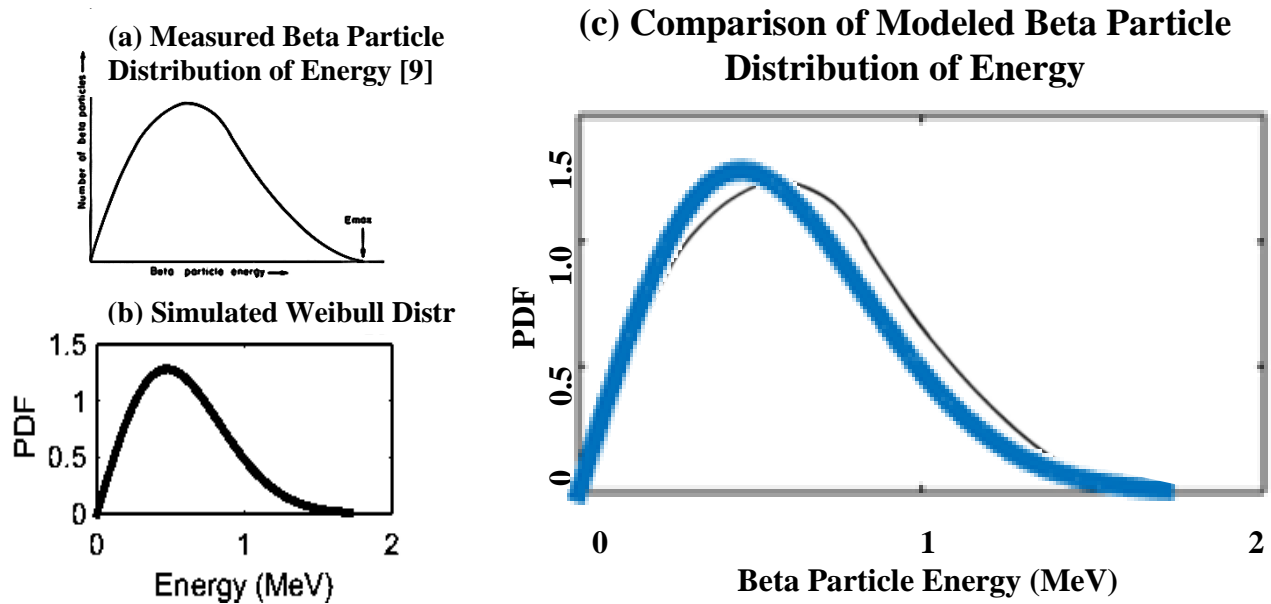


Figure A.1: Beta Particle Energy Distribution for (a) all beta particles, measured average, (b) simulated with Weibull Distribution, (c) shows the comparison

The energy distribution shown in (a) was experimentally measured and presented in Annunziata's Radioactivity textbook [9]. As shown in Figure A.1c, the Weibull distribution normalizes the probability density function from 0 to the maximum energy (1.7MeV) and slightly underestimates the energy distribution for values above the average. For the intentions of this project report, the Weibull Distribution with scale parameter 0.67, shape parameter 2.00, and mean 0.57 sufficiently represents ^{32}P emitted energy distribution.

2. Stopping Power

To detect a signal from a radiolabeled ADC, a beta particle must deposit some amount of energy on the sensor after experiencing energy loss and deflection after traveling through tissue. Energy loss is primarily due to inelastic collisions with electrons in the traveling medium and elastic scattering from radiative interaction with nearby nuclei [7]. These radiative and collisional losses are expressed through the stopping power, which defines the total energy lost per unit path length through a medium [7,21].

Radiative losses (bremsstrahlung) account for beta particle deflections and energy loss due to atomic interactions with other charged particles [17]. Bremsstrahlung is dominant for high energy beta particles, as higher excitation energies lead to stronger interactions with nearby atoms [17]. Collisional losses account for ionization that stem from interactions with orbital electrons in the medium [7]. During a collision, beta electrons collide with particles of identical mass (i.e. other electrons) which result in potentially large scattering angles of the beta particle. The total stopping power, described through the Bethe-Bloch formula, is outlined in the equation below [7]. It is given in [g/cm2] to express losses through different mediums [22]. The total energy lost in tissue is found by multiplying the stopping power with the density of tissue and distance traveled.

$$S(E_{initial}) = \frac{-dE}{dx_{total}} = \frac{-dE}{dx_{Radiative}} + \frac{-dE}{dx_{Collisional}}$$

$$S(\tau) = \frac{4\pi}{m_e c^2} \frac{k^2 z^2 e^4}{v^2} \frac{\rho Z N_A}{A} \left[\frac{1}{2} \ln\left(\frac{\tau^2(\tau+2)}{2(I/m_e c^2)^2}\right) + \frac{F(\tau)}{2} - \frac{\delta(v)}{2} - \frac{C(I, v)}{Z} \right]$$

$$\text{parameter from } S(E): \tau = E_{initial} / m_e c^2$$

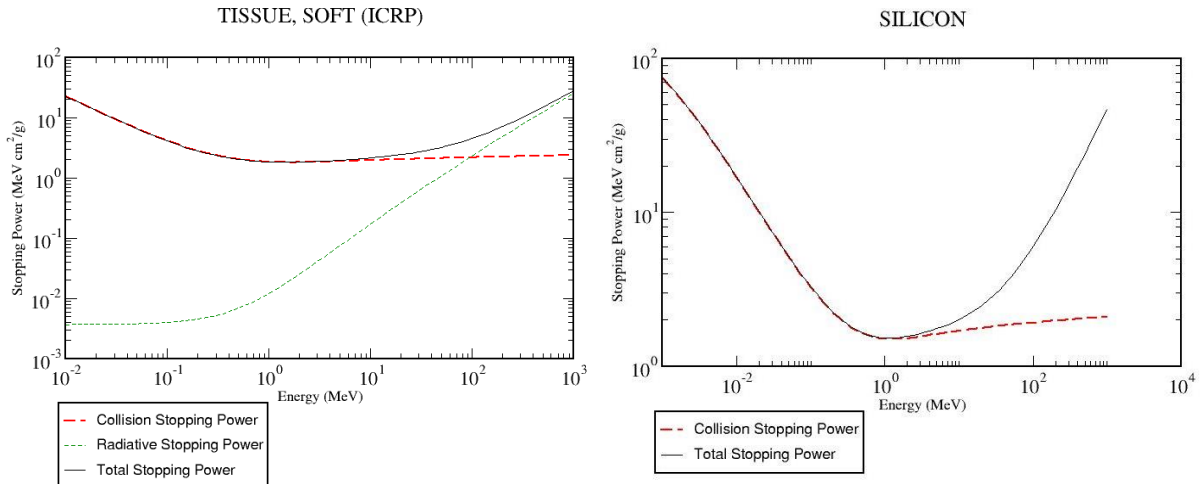


Figure A.2: Beta Electron Stopping Power in (a) Tissue and (b) Silicon [22]

Stopping power for a beta electron traveling through tissue is graphed in Figure A.2. From the equation, it is observed that the stopping power is dependent on the variable initial energy (expressed through τ). As seen in Figure 1.5, beta particles with an initial energy of $\sim 1\text{MeV}$ experience the lowest stopping power, while lower energy beta particles have a higher stopping power. Although minimizing the losses through the traveling medium is desirable, once the beta particle hits the sensor interface, higher collisional losses, which are reflected through a higher stopping power, are desired in order to ionize particles in the sensor and generate a measureable signal. For the case of a silicon sensor, the collisional stopping power (shown in Figure A.2b) follows a similar trend and is higher for lower energy beta particles [9].

References

- [1] McCance, K.; Huether, S.; Brashers, V.; Rote, N. "Biology, Clinical Manifestations, and Treatment of Cancer". *Pathophysiology The Biologic Basis for Disease In Adults and Children*. 6th edition. (2010): 360-395.
- [2] Friberk, S.; Mattson, S. "On the Growth Rates of Human Malignant Tumors: Implications for Medical Decision Making". *Journal of Surgical Oncology* 65 (1997): 284-97. *Bioquest*. BQ, Inc, 2009. Web. 17 Dec. 2015.
- [3] Tubiana, M.; Chauvel, P.; Renaud, A.; Malaise, E.P. "Vitesse De Croissance Et Histoire Naturelle Du Cancer Du Sein. Bulletin Du Cancer" (1975) 62:341–358.
- [4] Fournier, D.; Hoeffken, W.; Junkermann, H.; et al. "Growth rate of primary mammary carcinoma and its metastases". Zander J, Baltzer J (eds): "Early Breast Cancer." Berlin: Springer-Verlag, 1985.
- [5] Seo, D.; Carmena, J.M.; Rabaey, J.M.; Alon, E.; Maharbiz, M.M. (2014). "Model Validation Of Untethered, Ultrasonic Neural Dust Motes For Cortical Recording". *Journal of neuroscience methods*. 10 Feb 2015.
- [6] "Surveillance, Epidemiology, and End Results Program." Cancer of the Prostate. NCI Division of Cancer Control and Population Sciences. Web. 18 March. 2015.
- [7] Ganguly, T.; et. al. "A High Affinity 18F-Labeled Phosphoramidate Peptidomimetic PSMA-Targeted Inhibitor For PET Imaging Of Prostate Cancer" 20th ISRS Meeting, May 11-18, 2013.
- [8] Barbet, J.; Bardiès, M.; Bourgeois, M.; Chatal, J.; et.al. "Radiolabeled Antibodies for Cancer Imaging and Therapy." *Antibody Engineering*. New York City: Humana, 2012. 681-97. Print. Ser. 907.
- [9] Annunziata, M. F. "Beta Radiation." *Radioactivity Introduction and History*. Elsevier, 2007. 190-140. Print.
- [10] Cellere, G.; Larcher, L.; Paccagnella, A.; Visconti, A.; Bonanomi, M., "Radiation induced leakage current in floating gate memory cells," in *Nuclear Science, IEEE Transactions on* , vol.52, no.6, pp.2144-2152, Dec. 2005.
- [11] Menon, P. K. A.; Sridhar, B. "Passive Navigation using Image Irradiance Tracking" , AIAA Guidance, Navigation and Control Conference , 1989.
- [12] Young, S, K.; Cho, G.; Kwang, H. K.; Chi, Y. K. "Noise response in a CMOS active pixel sensor due to the radiation effects," in *Nuclear Science Symposium Conference Record, 2004 IEEE* , vol.3, no., pp.1640-1643 Vol. 3, 16-22 Oct. 2004.
- [13] Phillips, R; Milo, R. "How Big Is a Human Cell?" *Cell Biology by the Numbers Footer Comments*. BioNumbers, n.d. Web. 1 Dec. 2015.
- [14] Goodsell, D. S. "Molecular Machinery: A Tour of the Protein Data Bank". 2002, February. Web. 1 Dec. 2015.
- [15] Tian, Hui "Noise Analysis In Active CMOS Image Sensors". Stanford University, 2000. Print.
- [16] Gray, P. R; Hurst, P. J.; Lewis, S. H.; Meyer, R. G. "Analysis And Design Of Analog Integrated Circuits". Ed. Fifth. Wiley, 2010. 760-763. Print.
- [17] Seltzer, S.; Berger, S.M.; Martin J. "Bremsstrahlung Energy Spectra From Electrons With Kinetic Energy 1keV-10Gev Incident On Screen Nuclei And Orbital Electrons Of Neutral Atoms With $Z = 1-100^*$ ". *Atomic Data and Nuclear Data Tables*. Version 35, 345-418 (1986). Web 12 Dec 2014.
- [18] "Stopping Power and Range Tables for Electrons." National Institute Of Standards and Technology, Physics Measurement Laboratory, n.d. Web. 10 Dec. 2014.

- [19] Hawrysz, D.J; Sevick-Muraca, E.M. "Developments Toward Diagnostic Breast Cancer Imaging Using Near-Infrared Optical Measurements and Fluorescent Contrast Agents". *Neoplasia* (Sept-Oct 2000) Vol. 2, Iss. 5, 288-417. Elsevier. Web. 10 Dec 2015.
- [20] Li, Xu; Hagness, S.C., "A confocal microwave imaging algorithm for breast cancer detection," in *Microwave and Wireless Components Letters, IEEE* , Vol.11, no.3, 130-132, March 2001.